photonics

MDPI

Communication

Total Internal Reflection Lens for Optical Wireless Receivers

René Kirrbach *, Tobias Schneider, Mira Stephan, Alexander Noack, Michael Faulwaßer and Frank Deicke

Fraunhofer IPMS, Maria-Reiche-Straße 2, 01097 Dresden, Germany; tobias.schneider@ipms.fraunhofer.de (T.S.); mira.stephan@ipms.fraunhofer.de (M.S.); alexander.noack@ipms.fraunhofer.de (A.N.); michael.faulwasser@ipms.fraunhofer.de (M.F.); frank.deicke@ipms.fraunhofer.de (F.D.)
* Correspondence: rene.kirrbach@ipms.fraunhofer.de

Abstract: This work considers the use of a freeform total internal reflection (TIR) lens for optical concentration and provides for the first time experimental results in the context of optical wireless communications (OWC). The lens is placed on a surface-mounted device (SMD) avalanche photodiode (APD) to minimize position tolerances and simplify assembly. The lens achieves a concentration ratio of g_o = 44.7 (16.5 dB) within the FOV center and exhibits an acceptance angle of ±5°. The TIR lens approach is validated by comparing eye diagrams and bit error ratios (BER) of a receiver with and without a TIR lens. For the measurements, non-return-to-zero (NRZ) on-off keying (OOK) signals are transmitted with a data rate of 1.289 Gbit/s.

Keywords: free-space optics; FSO; freeform; LiFi; optical concentrator; optical wireless communications; OWC; ray tracing; receiver lens; TIR lens

check for updates

Citation: Kirrbach, R.; Schneider, T.; Stephan, M.; Noack, A.; Faulwaßer, M.; Deicke, F. Total Internal Reflection Lens for Optical Wireless Receivers. *Photonics* **2022**, *9*, 276. https://doi.org/10.3390/photonics9050276

Received: 28 March 2022
Accepted: 19 April 2022
Published: 20 April 2022

Publisher's Note: MDPI stays neutral with regard to jurisdictional claims in published maps and institutional affiliations.

1. Introduction

The growth of the mobile data traffic [1,2] challenges our wireless communication infrastructure. Moreover, new applications such as the tactile Internet [3,4] demand low-latency data transfer. Spatially well-confined optical wireless communication (OWC) channels are able to mitigate interference issues and allow for real-time data transfer with high reliability. Therefore, for certain applications, OWC can be an alternative to radio frequency-based technologies.

Optical wireless transceivers use photodiodes (PDs) such as P-i-N photodiodes (PIN PDs) [5] or avalanche photodiodes (APDs) [6]. To improve range and coverage, additional receiver lenses are used for optical concentration. For the sake of simplicity and cost, simple spherical and aspherical lenses have been used in industry and science [5,7–13]. A specific example is a hemispherical lens, which is well suited for large FOVs [11,13,14], [15] (pp. 103–104). The restricted shape of simple lenses limits design freedom and concentration ratio. For instance, it is barely possible to get a constant concentration ratio over the FOV with steep FOV edges. Moreover, large lenses are not suited for most practical applications due to their costly production. Freeform lenses have the potential to overcome these limitations of spherical lenses.

The concentration ratio of geometrical optics is limited by the conservation of Étendue [16] (pp. 18–22). Because fluorescence concentrators (FLC) can overcome the Étendue-caused concentration limit [17], there is high scientific interest in FLCs for OWC [17–22]. However, current FLCs limit the modulation bandwidth [23] and the gain for small FOVs. Therefore, FLCs surpass conventional concentrators only for large FOVs and modulation bandwidths well below 100 MHz. Consequently, there is still a need for geometrical ray optics such as high-performance freeform lenses.

Different freeform lenses have been studied over the last decades in the context of OWC. The compound parabolic concentrator (CPC) exhibits high efficiency and has been widely employed in science in various configurations [13,14], [15] (pp. 104–106). A successor of the CPC is the dielectric totally internally reflecting concentrator (DTIRC),

that was proposed in 1987 [24]. The main drawback of the CPC and the DTIRC is that their height and volume scale with increasing output aperture and decreasing acceptance angle [15] (pp. 104–122). Therefore, large PDs and small FOVs lead to bulky concentrators. Garcia Marquez et al. [25] and Valencia-Estrada et al. [26] described catadioptric lenses in 2015 and 2018, respectively. These lenses use at least one surface for refraction and TIR at the same time. Other works dealt with fisheye lenses [27] in 2014 and fly-eye lenses [28] in 2015. Moreover, there were practical and theoretical works on different hybrid transmitter-receiver lenses for low-range OWC [29,30] in 2018 and 2020, respectively. A TIR concentrator for OWC was proposed in 2019 [31]. However, the investigations were only theoretical and limited to simulations.

Although a growing interest in freeform lenses for OWC exists, there is a substantial lack of experimental data. Only a part of the works describes the concentrators in detail and only a few provide an experimental characterization. An experimental characterization is crucial for identifying relevant practical problems.

This paper considers freeform TIR lenses for OWC receivers. In this work, a lens prototype is fabricated and experimentally characterized. In contrast to previous works, we design the lens for a flat SMD package and mount it directly on top of it. For the first time, we show practical performance values in the context of OWC, as well as practical challenges and limits of the TIR lens approach.

The rest of the paper is organized as follows. Section 2 considers the concept of the TIR lens and the assembly. Section 3 presents the measurement setup and the results from the optical performance measurements and the data transfer experiment. The results are discussed in Section 4. Section 5 provides a summary.

2. Concept, Design, and Assembly

2.1. Concept

The optical concentration ratio g_{o} can be defined as the ratio of the detected power with the lens divided by the detected power without the lens. The maximum concentration ratio $g_{\mathrm{o\,max}}$ due to the conservation of Étendue can be expressed according to Equation (1) [16] (pp. 18–22). Therefore, $\boldsymbol{n}_1$ and $\boldsymbol{n}_2$ denote the refractive indices of the mediums at the concentrator's input and output. The angles θ_{in} and θ_{out} denote the maximum input and output angles, respectively.

$$g_{\mathrm{o\,max}} = \left(\frac{\boldsymbol{n}_2 \sin(\theta_{\mathrm{out}})}{\boldsymbol{n}_1 \sin(\theta_{\mathrm{in}})} \right)^2 \tag{1}$$

Figure 1 shows a cross-sectional concept render of the TIR lens and sketches incident rays for $-5°$, $0°$, and $+5°$ that reach the PD. The lens has a central refracting region and a surrounding TIR groove. TIR allows for larger deflection angles without large Fresnel losses in contrast to refraction [32]. Thus, it is suited to couple rays under larger angles θ_{out} to the PD chip. Therefore, the TIR lens has the potential to achieve a high concentration ratio.

In our setup, an APD is employed. However, the TIR lens is also compatible to other types of PDs. The PD features a cuboidal surface-mounted device (SMD) package. The PD chip has a diameter of 0.5 mm, which corresponds to an active area of approximately 0.2 mm^2. The chip is bonded onto a carrier and molded into a transparent polymer. The polymer top is flat. Because the polymer has no integrated lens, the receiver performance is prone to misalignments between the PD and the lens. Even a displacement of 200 µm takes a strong influence due to the small chip size. The problem is addressed by mounting the lens directly on the SMD package. For this purpose, the lens has mounting structures at the bottom that fit the SMD package. The mounting structures are located between the center and the TIR region. The size of the center region is determined by the SMD package. For handling and manufacturing, the lens features a cylindrical-shaped top. The flat top surface makes the lens robust against dirt particles.

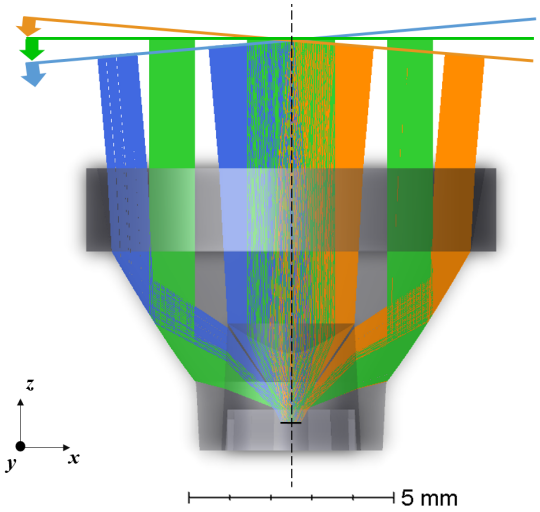

Figure 1. Cross-sectional concept render of the TIR lens and the PD. The colors indicate angles of incidence (blue: −5°, green: 0°, orange: +5°). Only rays that hit the PD chip are shown.

2.2. Geometrical Construction

Figure 2 illustrates the geometrical surface construction. The lens is designed by using the edge-ray principle and subsequent optimization of the angle of incidence $\theta_i = [\theta_a', \theta_a]$ to flatten g_o within the FOV. Therefore, θ_a denotes the acceptance angle and it holds $\theta_a' < \theta_a$. The construction procedure takes the flat PD surface into account. The interface is modeled with the parametric curve $\boldsymbol{C}(x)$. For this work, the curve is a simple straight line, where the parameter x refers to the x-coordinate. In general, the shape might be more complex and an arbitrary parameter might be chosen.

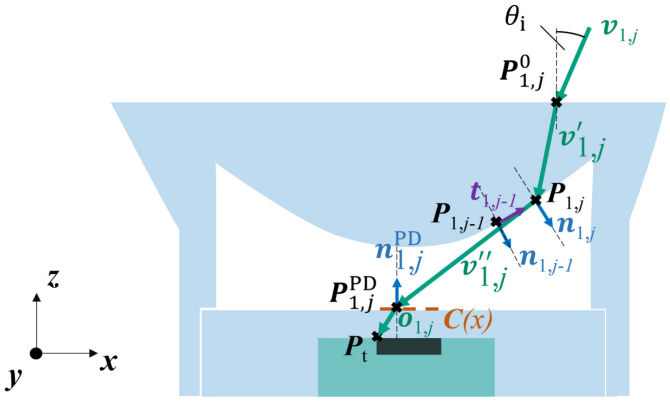

Figure 2. Geometrical construction of the lens surface.

Initially, the point $\boldsymbol{P}_{1,j}^0$ is defined. The input vector $\boldsymbol{v}_{1,j}$ is derived from the angle of incidence θ_i. The vector $\boldsymbol{v}_{1,j}'$ is calculated from $\boldsymbol{v}_{1,j}$ by the taking the refraction at the flat top surface into account. The point $\boldsymbol{P}_{1,j}$ is given by the intersection of $\boldsymbol{v}_{1,j}'$ and a tangential vector $\boldsymbol{t}_{1,j-1}$. The tangential vector $\boldsymbol{t}_{1,j-1}$ is derived by rotating the normal $\boldsymbol{n}_{1,j-1}$ of the previous point $\boldsymbol{P}_{1,j-1}$ around the y-axis by $\pi/2$. In general, it is not possible to directly calculate the normal vector $\boldsymbol{n}_{1,j}$, because the ray does not target the final point $\boldsymbol{P}_t$ directly. It is refracted at the PD package top at an unknown point $\boldsymbol{P}_{1,j}^{PD}$. The output vector $\boldsymbol{o}_{1,j}$ is unknown as well since it depends on $\boldsymbol{P}_{1,j}^{PD}$. The point $\boldsymbol{P}_{1,j}^{PD}$ is determined as follows: We define the law of refraction at the point $\boldsymbol{P}_{1,j}^{PD}$ according to Equation (2), where $\angle$ describes the angle between the vectors in the brackets. We assume $n_1 = 1$ and $n_2 = 1.5$.

$$n_1 \sin\left(\angle\left(\boldsymbol{v}_{1,j}'', \boldsymbol{n}_{1,j}^{PD}\right)\right) = n_2 \sin\left(\angle\left(\boldsymbol{o}_{1,j}, \boldsymbol{n}_{1,j}^{PD}\right)\right) \quad (2)$$

The problem is solved by expressing all variables as a function of $\boldsymbol{C}(x)$ and bringing the equation into the form $\boldsymbol{C}(x) = 0$. In the next step, the Newton algorithm is applied to extract the coordinate x_j. The point $\boldsymbol{P}_{1,j}^{\mathrm{PD}}$ corresponds to $\boldsymbol{C}(x_j)$. The vectors $\boldsymbol{o}_{1,j}$ and $\boldsymbol{v}_{1,j}''$ are given by $\boldsymbol{o}_{1,j} = \boldsymbol{P}_{\mathrm{t}} - \boldsymbol{C}(x_j)$ and $\boldsymbol{v}_{1,j}'' = \boldsymbol{C}(x_j) - \boldsymbol{P}_{1,j}$. The normal vector $\boldsymbol{n}_{1,j}^{\mathrm{PD}}$ is the rotated tangential vector of the function $\boldsymbol{C}(x = x_j)$ according to Equation (3).

$$\boldsymbol{n}_{1,j}^{\mathrm{PD}} = \boldsymbol{R}_{\alpha}\left(\frac{\pi}{2}\right) \cdot \frac{\partial \boldsymbol{C}(x = x_j)}{\partial x} \tag{3}$$

Thus, $\boldsymbol{R}_{\alpha}(\pi/2)$ denotes the rotation matrix. For a simple flat SMD package, $\boldsymbol{n}_{1,j}^{\mathrm{PD}}$ is parallel to the z-axis. After $\boldsymbol{P}_{1,j}^{\mathrm{PD}}$ is known, $\boldsymbol{v}_{1,j}''$ and $\boldsymbol{o}_{1,j}$ are calculated. By using this procedure, a 2D curve of the lens is generated. The number of calculated points per curve N is 1200. The calculated curves are interpolated using cubic non-uniform rational basis splines (NURBS) [32]. A 3D representation is generated by rotating the curve around the z-axis. A render image of the design is shown in Figure 1.

2.3. Frabication and Assembly

Figure 3 shows a lens prototype. It is fabricated with an injection molding process. The tool was formed by an ultra-precision diamond-turning/-milling process. The milling tip features a radius of 100 µm. The surface roughness is classified as SPI A-2, i.e., the optical interfaces have an average surface roughness R_{a} of 25 nm to 50 nm. The lens material is black polycarbonate with a refractive index of $n = 1.57$. The material absorbs ambient light for $\lambda < 700$ nm and provides a high transmittance of $T > 0.9$ for $\lambda > 800$ nm. This makes the material an ideal candidate for near-infrared (NIR) signals. The lens has a height of 6.9 mm and an optical input aperture of Ø8.8 mm. The planarity of the top surface can be seen from the reflection. The diameter of the lens cavity is 3.1 mm. The inner sides of the cavity are inclined by 2°, which is required for the diamond-turning.

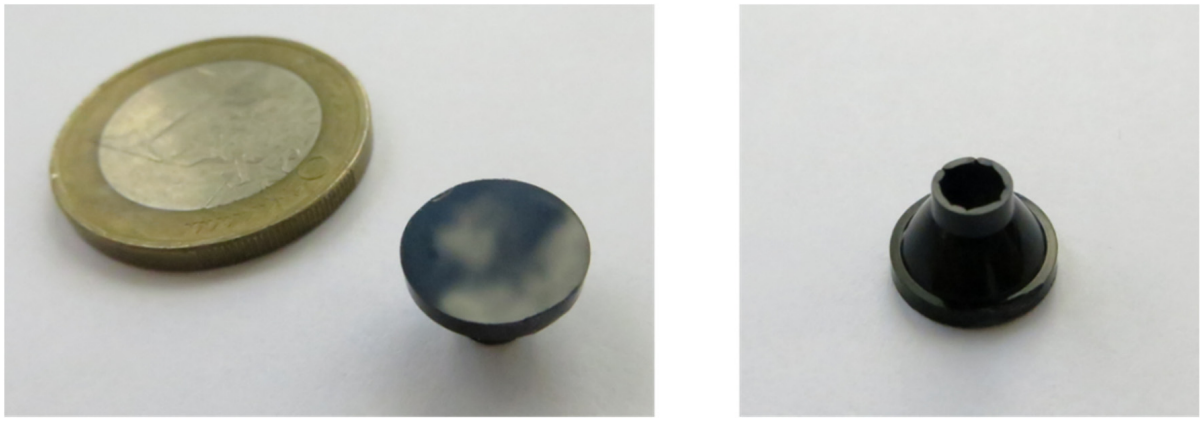

Figure 3. TIR lens prototype. (**a**) Perspective top view. (**b**) Perspective bottom view.

The lens is fixed to the PD by using a low-outgassing adhesive, which is transparent at the wavelength of communication. Because the glue is not applied to the top of the PD, the glue does not necessarily have to be transparent. However, it must be low-outgassing to avoid an undesired covering of the lenses' center cavity. When the lens is placed on the PD, it wiggles slightly, indicating that the mounting structures do not fit exactly. This issue can be eliminated by a selective revision of the tool.

3. Measurements

3.1. Optical Setup

Figure 4 shows a sketch of the measurement setup. A LED is placed at a distance of Z_o = 600 mm in front of the receiver. The LED features a center wavelength of 850 nm and an optical output power of 260 mW. The optical receiver is rotated around the y-axis by an angle θ_i. To remove the residual influence of the LED profile, we measure the photocurrent I_{PD} over θ_i with and without the TIR lens and define g_o as the ratio of both results. For the I_{PD} measurement, we measure the voltage drop over a resistor in series to the APD with the multimeter *Keysight U1272A*. We temporally deactivate the APD bias to avoid corruption by the APD's avalanche effect (M = 1). The optical power is derived from I_{PD} by using the PD responsivity R = 0.5 A/W. The optical power with lens divided by center power without the lens is defined as the optical concentration ratio g_o. The small angular error resulting from the distance between the lens surface and the axis of rotation is taken into account during the measurements.

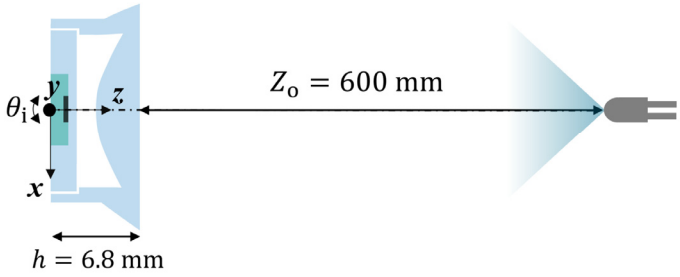

Figure 4. Measurement setup for the optical concentration ratio g_o.

3.2. Optical Results

Figure 5a shows the results of the I_{PD} measurement. The photodiode without the lens shows quite similar I_{PD} values for the observed θ_i. In contrast, the TIR lens shows a strong dependence from θ_i. It increases I_{PD} within the center from 303 nA without the lens to 13.55 µA.

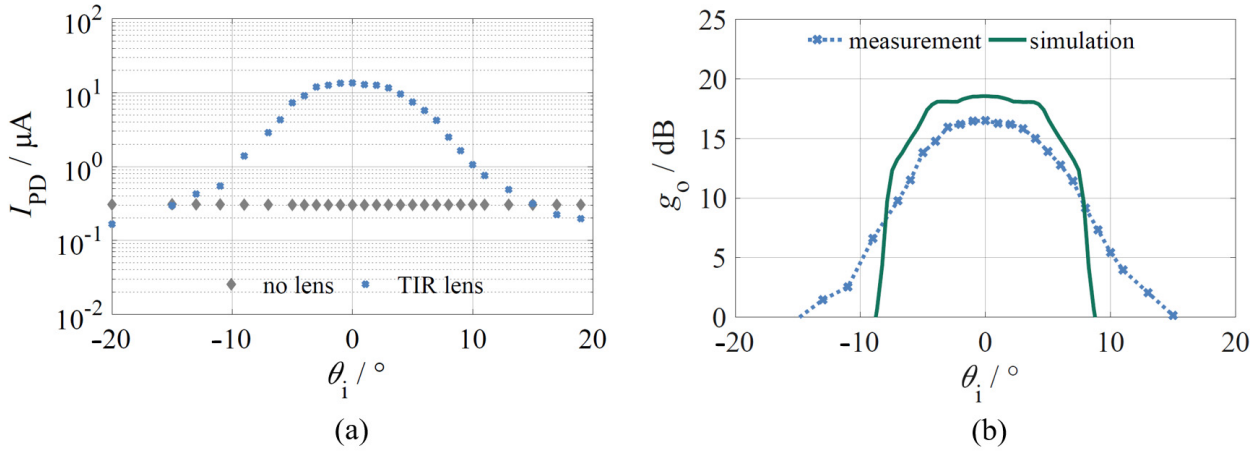

Figure 5. (**a**) Measured photocurrent I_{PD} with and without the TIR lens. (**b**) Measured and simulated concentration ratio g_o.

Figure 5b shows the simulated and measured optical concentration ratio g_o over the angle of incidence θ_i. The simulation is based on Monte Carlo ray tracing within *Zemax Optic Studio 17*. For each simulation point, 10^6 rays are traced. The simulated lens features a center gain of up to 18.5 dB and enables data reception for $\theta_i < 7.5°$. For larger angles, the gain drops rapidly. The simulated acceptance angle (−3 dB) is θ_a^{sim} = 5.5°. From the experiment, we derive a concentration ratio of g_o = 10lg (44.7) = 16.5 dB at the center, which

is 2 dB lower than the simulation. The measured curve has an acceptance angle of $\theta_a^m = \pm 5°$. Moreover, it drops slower outside the FOV compared to the simulated curve.

Within our laboratory, the ambient light is 38 nA without the TIR lens and 0.8 nA with the TIR lens. This corresponds to an attenuation of ambient light by 16.8 dB.

3.3. Data Transmission Setup

Figure 6 shows the experimental setup for data transmission. For the validation of the TIR lens, we transmit a non-return-to-zero (NRZ) on-off keying (OOK) signal through an optical wireless channel with and without the TIR lens. This is close to the baud rate of 8B/10B-coded 1000BASE-T networks that are highly relevant for industrial real-time communication protocols. A *Stratix V* field-programmable gate array (FPGA) is used to generate a pseudo-random bit sequence (PRBS-7) at the transmitter. The transmitter converts the signal into the optical domain. Thus, a custom laser driver converts the voltage signal from the FPGA into a current and directly drives an edge-emitting laser diode (LD) to modulate the optical intensity. The center wavelength of the LD is 850 nm. The receiver printed circuit board (PCB) contains an APD for signal detection. The APD bias is varied within a control loop to adjust the APD gain depending on the incident optical power. For strong input signals, the bias and thus the APD gain is reduced to avoid saturation. The photocurrent is converted into a voltage using a transimpedance amplifier (TIA). The eye diagram is measured using a digital oscilloscope of type *Lecroy 10-36Zi*. The *Stratix V* FPGA is used to carry out a bit error rate test (BERT) at the receiver. The measurements are repeated for Z_o = 50 cm, Z_o = 100 cm and Z_o = 150 cm with and without the TIR lens. Table 1 summarizes the optical wireless link parameters.

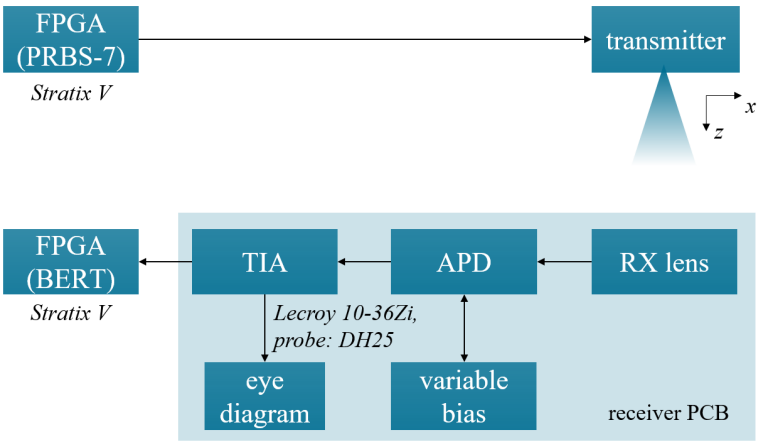

Figure 6. Experimental setup for the eye diagram and BER measurements.

Table 1. Parameters of the optical wireless link.

Parameter	Symbol	Value	Unit
Wavelength	λ	850	nm
Calculated points	N	1200	per surface
PD	-	Si-APD	-
PD diameter	d_{PD}	0.5	mm
Responsivity (M = 1)	R	0.5	A/W
Lens input diameter	d_l	8.8	mm
Acceptance angle	θ_a^m	± 5	°
Calculated points	N	1200	per surface
Bit rate	R	1.289	Gbit/s
Modulation	-	NRZ-OOK	-
Pattern	-	PRBS-7	-
Probe bandwidth	f_{probe}	13	GHz

3.4. Data Transmission Results

Figure 7a–c show the measured eye diagrams for the channel without the lens and Figure 7d–f for the channel with the lens. Table 2 lists the BERT data. The BER measurement is clipped at 10^{-12}, when no bit errors occurred after 1000 s. For all measurements, the eye opening increases with a TIR lens. The improvement varies with the received signal power and thus the APD bias that is adjusted to avoid saturation. The improvement is clearly visible for rather high distances with a weak input signal. For instance, at Z_o = 150 cm, there is practically an error-free transmission with the TIR lens, but no transmission at all without it. The avalanche effect leads to stronger noise at the high level compared to the low level [33] (pp. 58–60). This can be seen in particular for the weak signals in Figure 7b,c, where the APD gain is high.

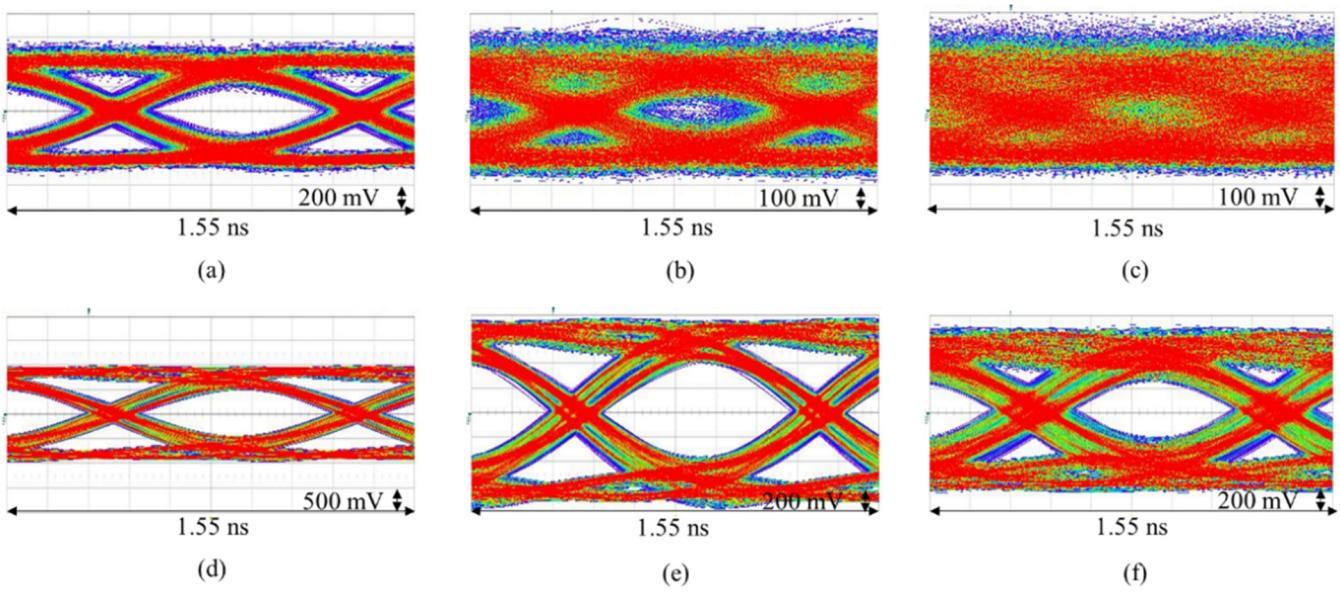

Figure 7. Eye diagrams for PRBS-7 signals with a bit rate of 1.289 Gbit/s. (**a**) No lens (Z_o = 50 cm), (**b**) no lens (Z_o = 100 cm), (**c**) no lens (Z_o = 150 cm), (**d**) with lens (Z_o = 50 cm), (**e**) with lens (Z_o = 100 cm), (**f**) with lens (Z_o = 150 cm). The observed bandwidth is 3 GHz.

Table 2. Numerical results of the BERT.

Configuration	TIR Lens	Z_o	BER
a	no	50 cm	$<10^{-12}$
b	no	100 cm	3×10^{-4}
c	no	150 cm	3×10^{-2}
d	yes	50 cm	$<10^{-12}$
e	yes	100 cm	$<10^{-12}$
f	yes	150 cm	$<10^{-12}$

4. Discussion

4.1. Performance

The measurement from Figure 5b shows a high concentration ratio of 44.7 (16.5 dB) despite the small form factor of the lens. The eye diagram measurements and the BERT prove that the optical concentration improves the data transmission drastically. In our tests, the TIR lens increased the eye opening, thereby improving the BER. The eye opening is not directly proportional to the optical concentration ratio due to adjusted APD gain. The range measurements were limited by our optical bench to a maximum distance of 150 cm. At a first approximation, a concentration ratio of 44.7 corresponds to a range improvement by a factor of approximately $\sqrt{44.7} \approx 6.7$.

Nevertheless, the measured values are well below the simulation values according to Figure 5b. The shift of the profile and the fact that the mounting structures did not fit perfectly indicate that there is a misalignment between the lens and the PD chip. Because the gain falls slower outside the FOV than simulated, it is likely that the focus point of the lens is larger than intended, which could be caused by an additional z-displacement between lens and PD. A part of those deviations is caused by the finite shape accuracy of the tooling process and roundings at the edges of the surfaces. A precise analysis is challenging and costly, especially for the inner surfaces of the cavity. Therefore, such analyses are out of the scope of this work. A rework of the mounting structures is one way to reduce the position tolerances. However, the final position accuracy also depends on the spatial tolerances of the SMD packages. Those are typically in the range of a few hundredths of µm due to the sawing process that is used for device separation. Active positioning is another possibility to address the mechanical tolerances. However, this makes the fabrication more complex and thus is not desired for mass fabrication.

A significant drawback of our setup is the flat surface of the SMD package. In contrast to a package with an integrated convex lens, the optical concentration ratio is reduced, because the flat surface reduces the angular acceptance region and the TIR lens cannot fully profit from the higher refractive index $\boldsymbol{n}_2$ of the PD package surrounding the active chip according to Equation (1). Moreover, an integrated lens would further reduce the influence of a displacement between the lens and the PD chip.

4.2. Comparison with CPC and DTIRC

The planar SMD package might be suited for a CPC or DTIRC. Compared to a DTIRC, the TIR lens covers the PD chip completely and reduces the ambient light photocurrent to a minimum by material absorption. The CPC and DTIRC most likely achieve a higher concentration ratio due to the direct contact to the PD package. Nevertheless, they feature challenges including precise alignment, the need for an index matching gel, and excess glue at the output aperture. Moreover, CPCs and DTIRC are higher and might not be suited for all applications. For the present setup, a realistic height is in the range of multiples of tens of millimeters depending on the realization. In comparison, the presented TIR lens is a compact concentrator with height of only 6.9 mm. It seems especially favorable for PD packages with non-flat surfaces, such as packages with integrated lenses that are not suited for the CPC or DTIRC. It allows for an easy assembly because the glue is not applied into the ray path and there is no issue with excess glue. The flat top of the TIR lens enables integration into a transceiver case without the need for an additional front plate.

5. Conclusions

This article considers the design and experimental characterization of a freeform TIR lens as an optical concentrator for OWC receivers. The experimental characterization of the lens prototype provides practical performance merits for the first time in the context of OWC and proves the general feasibility for data transmission. The proposed TIR lens is a compact concentrator with an entrance aperture of Ø8.8 mm and a height of only h = 6.9 mm. It fits on a cuboidal SMD package and requires no index-matching gel or glue within the optical path. Therefore, it simplifies the assembly compared to a corresponding CPC. The acceptance angle θ_a of the prototype is $\pm 5°$. It achieves a concentration ratio of g_o = 44.7 (16.5 dB) within the FOV center. Small concentrators such as the proposed TIR lens require precise positioning. The investigations suggest that more precise mounting structures can improve the assembly. One drawback of the TIR lens is the complex lens structure that makes the characterization of the shape accuracy difficult, especially within the lens cavity.

Author Contributions: Conceptualization, R.K. and T.S.; data curation, R.K.; formal analysis, R.K.; investigation, R.K. and T.S.; methodology, R.K.; project administration, A.N. and F.D.; resources, R.K.; software, R.K.; supervision, A.N. and F.D.; validation, R.K. and T.S.; visualization, R.K.; writing—original draft, R.K.; writing—review and editing, R.K., T.S., M.S., A.N., M.F. and F.D. All authors have read and agreed to the published version of the manuscript.

Funding: This research received no external funding.

Institutional Review Board Statement: Not applicable.

Informed Consent Statement: Not applicable.

Data Availability Statement: Not applicable.

Conflicts of Interest: The authors declare no conflict of interest.

References

1. Winzer, P.J.; Neilson, D.T. From Scaling Disparities to Integrated Parallelism: A Decathlon for a Decade. *J. Lightwave Technol.* **2017**, *35*, 1099–1115. [CrossRef]
2. Cerwall, P.; Ramiro, J.; Outes, J.; Bhardwaj, A.; Muñiz Garcia, C.; Baur, H.; Alger, J.; Krautkremer, T.; Chandra, R.; Lundborg, T.; et al. Ericsson Mobility Report: June 2021. Available online: https://www.ericsson.com/49cd40/assets/local/mobility-report/documents/2021/june-2021-ericsson-mobility-report.pdf (accessed on 16 June 2021).
3. Fitzek, F.H.P.; Li, S.-C.; Speidel, S.; Strufe, T.; Simsek, M. (Eds.) *Tactile Internet: With Human-In-the-Loop*; Elsevier AP Academic Press: Cambridge, MA, USA, 2021; ISBN 0-12-821343-4.
4. Szabo, D.; Gulyas, A.; Fitzek, F.H.P.; Lucani, D.E. Towards the Tactile Internet: Decreasing Communication Latency with Network Coding and Software Defined Networking. In Proceedings of the European Wireless 2015; 21th European Wireless Conference, Budapest, Hungary, 20–22 May 2015; pp. 1–6.
5. Brandl, P.; Zimmermann, H. Optoelectronic integrated circuit for indoor optical wireless communication with adjustable beam. In Proceedings of the 2013 18th European Conference on Network and Optical Communications & 2013 8th Conference on Optical Cabling and Infrastructure (NOC-OC&I), Graz, Austria, 10–12 July 2013; pp. 149–152.
6. O'Brien, D.; Turnbull, R.; Le Minh, H.; Faulkner, G.; Bouchet, O.; Porcon, P.; El Tabach, M.; Gueutier, E.; Wolf, M.; Grobe, L.; et al. High-Speed Optical Wireless Demonstrators: Conclusions and Future Directions. *J. Lightwave Technol.* **2012**, *30*, 2181–2187. [CrossRef]
7. Chun, H.; Rajbhandari, S.; Tsonev, D.; Faulkner, G.; Haas, H.; O'Brien, D. Visible light communication using laser diode based remote phosphor technique. In Proceedings of the 2015 IEEE International Conference on Communication Workshop (ICCW), London, UK, 8–12 June 2015; pp. 1392–1397, ISBN 2164-7038.
8. Yeh, C.-H.; Lu, I.-C. 0.52–11.86 Gbit/s OFDM modulation for power-sharing VLC transmission by using VCSEL laser. *Opt. Express* **2016**, *24*, 21113–21118. [CrossRef] [PubMed]
9. Li, X.; Bamiedakis, N.; Guo, X.; McKendry, J.J.D.; Xie, E.; Ferreira, R.; Gu, E.; Dawson, M.D.; Penty, R.V.; White, I.H. Wireless Visible Light Communications Employing Feed-Forward Pre-Equalization and PAM-4 Modulation. *J. Lightwave Technol.* **2016**, *34*, 2049–2055. [CrossRef]
10. Hussein, A.F.; Elgala, H.; Fahs, B.; Hella, M.M. Experimental investigation of DCO-OFDM adaptive loading using Si PN-based receiver. In Proceedings of the 2017 26th Wireless and Optical Communication Conference (WOCC), Newark, NJ, USA, 7–8 April 2017; ISBN 978-1-5090-4909-7.
11. Yu, B.; Liang, S.; Ding, X.; Yang, Y.; Shao, C.; Zhao, Q.; Li, Z. Performance Investigation on Hemispherical Lens used in Photodetector for Visible Light Communications. In Proceedings of the 2019 20th International Conference on Electronic Packaging Technology(ICEPT), Hong Kong, China, 12–15 August 2019; pp. 1–4, ISBN 978-1-7281-5064-2.
12. Faulwaßer, M.; Deicke, F.; Schneider, T. 10 Gbit/s bidirectional optical wireless communication module for docking devices. In Proceedings of the 2014 IEEE Globecom Workshops (GC Wkshps), Austin, TX, USA, 8–12 December 2014; pp. 512–517, ISBN 2166-0077.
13. Wang, Y.; Lan, T.; Ni, G. Optical receiving system based on a compound parabolic concentrator and a hemispherical lens for visible light communication. *Appl. Opt.* **2016**, *55*, 10229–10238. [CrossRef]
14. Kahn, J.M.; Barry, J.R. Wireless Infrared Communications. *Proc. IEEE* **1997**, *85*, 265–298. [CrossRef]
15. Ramirez-Iniguez, R.; Idrus, S.M.; Sun, Z. *Optical Wireless Communications: IR for Wireless Connectivity*; Auerbach Publications: Boca Raton, FL, USA, 2008; ISBN 978-0367452674.
16. Winston, R.; Miñano, J.C.; Benítez, P. *Nonimaging Optics*; Elsevier Academic: Amsterdam, The Netherlands, 2005; ISBN 9780127597515.
17. Collins, S.; O'Brien, D.C.; Watt, A. High gain, wide field of view concentrator for optical communications. *Opt. Lett.* **2014**, *39*, 1756–1759. [CrossRef]

18. Collins, S.; Mulyawan, R.; Rajbhandari, S.; Chu, H.; Faulkner, G.E.; O'Brien, D.C.; Manousiadis, P.P.; Vithanage, D.A.; Turnbull, G.A.; Samuel, I.D.W. A simple wide field of view concentrator for free space visible light communications. In Proceedings of the 2015 IEEE Photonics Society Summer Topical Meeting Series (SUM), Nassau, Bahamas, 13–15 July 2015; pp. 43–44, ISBN 978-1-4799-7468-9.
19. Collins, S. Smart Phones: An example application for fluorescent concentrators. In Proceedings of the 2019 Global LIFI Congress (GLC), Paris, France, 12–13 June 2019; pp. 1–4, ISBN 978-1-7281-5022-2.
20. Manousiadis, P.P.; Rajbhandari, S.; Mulyawan, R.; Vithanage, D.A.; Chun, H.; Faulkner, G.; O'Brien, D.C.; Turnbull, G.A.; Collins, S.; Samuel, I.D. Wide field-of-view fluorescent antenna for visible light communications beyond the étendue limit. *Optica* **2016**, *3*, 702. [CrossRef]
21. Peyronel, T.; Quirk, K.J.; Wang, S.C.; Tiecke, T.G. Luminescent detector for free-space optical communication. *Optica* **2016**, *3*, 787. [CrossRef]
22. Yu, B.; Liang, S.; Ding, X.; Li, Z.; Tang, Y. A Sandwich Structure Light-Trapping Fluorescence Antenna With Large Field of View for Visible Light Communication. *IEEE Trans. Electron Devices* **2021**, *68*, 565–571. [CrossRef]
23. Portnoi, M.; Haigh, P.A.; Macdonald, T.J.; Ambroz, F.; Parkin, I.P.; Darwazeh, I.; Papakonstantinou, I. Bandwidth limits of luminescent solar concentrators as detectors in free-space optical communication systems. *Light Sci. Appl.* **2021**, *10*, 3. [CrossRef] [PubMed]
24. Ning, X.; Winston, R.; O'Gallagher, J. Dielectric totally internally reflecting concentrators. *Appl. Opt.* **1987**, *26*, 300–305. [CrossRef] [PubMed]
25. Garcia-Marquez, J.; Valencia, J.C.; Perez, H.; Topsu, S. Catadioptric lenses in Visible Light Communications. *J. Phys. Conf. Ser.* **2015**, *605*, 12029. [CrossRef]
26. García-Márquez, J.; Valencia-Estrada, C.; Topsu, S.; Chassagne, L. Optical antenna for a visible light communications receiver. In *Broadband Access Communication Technologies XII, Proceedings of SPIE Volume 10559, San Francisco, CA, USA, 27 January–1 February 2018*; Dingel, B.B., Tsukamoto, K., Mikroulis, S., Eds.; SPIE: Bellingham, WA, USA, 2018; p. 20, ISBN 9781510616035.
27. Chen, T.; Liu, L.; Tu, B.; Zheng, Z.; Hu, W. High-Spatial-Diversity Imaging Receiver Using Fisheye Lens for Indoor MIMO VLCs. *IEEE Photon. Technol. Lett.* **2014**, *26*, 2260–2263. [CrossRef]
28. Tang, X.; Pan, D.; Zhang, X.; Xi, L.; Zhang, W. A novel receiver employing a compound-eye lens and a frequency domain synchronization algorithm for multiple-input single-output visible light communication system. In Proceedings of the 2015 14th International Conference on Optical Communications and Networks (ICOCN), Nanjing, China, 3–5 July 2015; ISBN 978-1-4673-7373-9.
29. Faulwaßer, M.; Kirrbach, R.; Schneider, T.; Noack, A. 10 Gbit/s bidirectional transceiver with monolithic optic for rotary connector replacements. In Proceedings of the 2018 Global LIFI Congress, Paris, France, 8–9 February 2018; pp. 95–102.
30. Kirrbach, R.; Faulwaßer, M.; Schneider, T.; Meißner, P.; Noack, A.; Deicke, F. Monolitic Hybrid Transmitter-Receiver Lens for Rotary On-Axis Communications. *Appl. Sci.* **2020**, *10*, 1540. [CrossRef]
31. Kirrbach, R.; Jakob, B.; Noack, A. Introducing Advanced Freeform Optic Design to Li-Fi Technology. In Proceedings of the 7th International Conference on Photonics, Optics and Laser Technology, Prague, Czech Republic, 25–27 February 2019; pp. 2184–4364. [CrossRef]
32. Wallhead, I.; Jiménez, T.M.; Ortiz, J.V.G.; Toledo, I.G.; Toledo, C.G. Design of an efficient Fresnel-type lens utilizing double total internal reflection for solar energy collection. *Opt. Express* **2012**, *20*, A1005–A1010. [CrossRef] [PubMed]
33. Säckinger, E. *Analysis and Design of Transimpedance Amplifiers for Optical Receivers*; John Wiley & Sons, Inc.: Hoboken, NJ, USA, 2017; ISBN 9781119264422.